PAPER

Damage characterization of heat-treated titanium bio-alloy (Ti–6Al–4V) based on micromechanical modeling

To cite this article: Shima Rastgordani *et al* 2020 *Surf. Topogr.: Metrol. Prop.* **8** 045016

Surface Topography: Metrology and Properties

PAPER

Damage characterization of heat-treated titanium bio-alloy (Ti–6Al–4V) based on micromechanical modeling

RECEIVED
11 June 2020

REVISED
1 September 2020

ACCEPTED FOR PUBLICATION
14 October 2020

PUBLISHED
21 October 2020

Shima Rastgordani[1], **Ali Ch Darabi**[2], **Javad Kadkhodapour**[1], **Seyed Reza Hamzeloo**[1], **Mohammadreza Khoshbin**[1], **Siegfried Schmauder**[2] and **Javad Mola**[3]

[1] Department of Mechanical Engineering, Shahid Rajaee Teacher Training University, Tehran, Iran
[2] Institute of Materials Testing, Materials Science and Strength of Materials (IMWF), University of Stuttgart, Stuttgart, Germany
[3] Materials Design and Structural Integrity Laboratory, Faculty of Engineering and Computer Sciences, Osnabrück University of Applied Sciences, 49076, Osnabrück, Germany

E-mail: Shimarastgordani@gmail.com

Keywords: dual-phase titanium, Ti–6Al–4V, GTN damage model, Taguchi method, micromechanical modeling, biomedical applications

Abstract

In this study, a micromechanical finite element model is proposed based on experimental data and the rule of the mixture (RoM) in order to predict the tensile behavior of mechanical properties of heat-treated dual-phase medical-grade titanium (Ti–6Al–4V). Tensile tests, micro-hardness measurements, and RoM were used to obtain flow curves for the α and β phases. Scanning electron microscopy (SEM) imaging was used to determine phase fractions and to create representative volume elements (RVEs). Furthermore, the Gurson-Tvergaard-Needleman (GTN) damage model was calibrated using the Taguchi design of experiment (DOE) method in order to predict damage in the microstructure and the results were compared to fracture surface obtained using fractography in order to investigate failure mechanisms. The final micromechanical model could accurately predict stress-strain curves and showed that void formation and coalescence is the primary mechanism of failure. Finally, analyses of the surfaces showed that a fully ductile fracture occurs at the failure point, which agrees with the results of the damage model. The results suggest that the proposed model can predict the failure of heat-treated Ti–6Al–4V bio-alloys.

1. Introduction

Biocompatibility, high corrosion resistance, high specific strength, and low density are the most critical features of Ti–6Al–4V alloys, also known as 'Titanium grade 5' [1]. These properties make this alloy the most attractive titanium alloy in biomedical industries, marine and petrochemical applications, as well as the transportation industry [1–5].

Microstructures, and subsequently, the mechanical properties are influenced by the heat treatment process, especially in titanium alloys [6]. Many recent studies are dedicated to the effects of heat treatment on microstructure evolution and phase transformation in additively manufactured Ti–6Al–4V alloy [7–10], which highlights the necessity of further research efforts, especially a survey on the damage characterization of heat-treated, 3D printed Ti–6Al–4V via micromechanical modeling.

Although there have been widespread micromechanical investigations on different metals with dual and multi-phase microstructures, particularly different steel grades [11–14], not many studies focused on the optimization of the mechanical performance of titanium alloys using insights from the finite element method. The dual-phase microstructure of Ti–6Al–4V alloy makes it very suitable for micromechanical analysis. Ti–6Al–4V alloys consist of a microstructure with a softer matrix (α phase) with a harder phase, known as the β phase. The size, morphology, and volume fraction of the β phase rely on the production process, particularly on the annealing temperature and the heat treatment process [15].

It has been established in the literature that hardness (H) and flow stress (σ) are related using the expression $H(\varepsilon) = C\sigma(\varepsilon)$ where C is strain-independent under some test conditions [16, 17]. This relationship has been successfully used to estimate the

Table 1. The chemical composition of Ti–6Al–4V alloy used in this study (wt%).

Ti	Al	V	Fe	C	N	O	H
Balance	5.82	3.92	0.09	0.011	0.003	0.12	0.012

yield stress in steels [18, 19]. Furthermore, the RoM has been used to establish a relationship between the hardness of the phases and that of the alloy. Due to the linear relationship between hardness and flow stress, the RoM can also be used for predictions of the flow stress [20].

The Gurson–Tvergaard–Needleman (GTN) damage model [21] is a ductile failure criterion which has been used to study failure mechanism in many metals [22–25], including titanium alloys [26–28]. The GTN model considers nucleation, growth, and coalescence of micro-voids and void volume fraction, which can give a suitable view of the damage in a material [29]. Recently, the calibration of GTN parameters in order to accurately predict the damage mechanisms has seen increased attention. In order to have a successful calibration and to reduce the number of trials, the design of experiment (DOE) methods and, in particular, the Taguchi method has been effectively applied to mechanical studies [30–34].

To the best of the authors' knowledge, no comprehensive research exists on the effect of heat-treatment on the GTN damage mechanisms of Ti–6Al–4V alloy and following its micro-mechanical characteristics. In this study, aging heat-treatment was performed as it was found more beneficial due to enhancing larger β grains [35], subsequently higher yield stress among all the heat treatment conditions examined by Li *et al* [36]. Furthermore, to validate damage simulations, the material was characterized experimentally using scanning electron microscopy (SEM), hardness measurements, and tensile testing. Experimental data were used to perform two-dimensional (2D) micro-mechanical finite element (FE) simulations in the representative volume element (RVE) framework. Finally, the GTN damage model was calibrated using the Taguchi DOE approach and used to analyze damage initiation and failure mechanisms in a cold-rolled aged Ti–6Al–4V alloy.

2. Materials and methods

2.1. Materials

A commercially cold-rolled and annealed sheet of 2.00 mm thick Ti–6Al–4V alloy with the chemical composition given in table 1, was aged at 550 °C for eight hours and air-cooled.

The heat-treated samples were prepared for hardness testing and SEM images according to the ASTM E3-17 standard. They were wet-ground with 120, 220, 600, 1000, 1200, 1500, 1800, and 2000 grit SiC papers, and subsequently polished via a 0.25 μm alumina suspension. Samples were then etched by Kroll's reagent in a solution consisting of 5% HF, 10% HNO_3, and H_2O before SEM observations. The SEM image can be seen in figure 3(a) with the gray areas being the α phase and the white areas, which represent the β phase with 15.2% of volume fraction.

Tensile test specimens were prepared according to DIN50125 standard, and uniaxial tensile tests were performed at room temperature with a strain rate of $1.6 \times 10^{-4}\,s^{-1}$. The tests were repeated three times to account for repeatability. The elastic-plastic portions of engineering stress-strain curves are plotted in figure 1.

In addition, using backscattered electron imaging, the microstructure of both as-received and aged samples have been depicted in figures 1(b) and (c), respectively. The bimodal $\alpha + \beta$ equiaxed microstructure could be observed in the images [37]. Regarding the air cooling process, In figure 1(c), the β grain boundaries are clearly revealed by a wide α layer. These large alpha lamellae could also be depicted due to the aging heat treatment [38].

2.2. Micro-hardness measurements

Micro-indentation testing was performed according to DIN EN ISO 14577-1 using a FISCHERSCOPE HM2000 on the as-received and aged Ti–6Al–4V alloy in order to measure the mechanical properties of the α and β phases. A maximum indentation load of 40 mN was reached within 14 s and held for 5 s before unloading for 14 s.

A total of 85 valid measurements were taken in various points of the microstructure, some of which were near phase boundaries. It is evident from the work of Kadkhodapour *et al* [39] that the hardness changes in the vicinity of phase and grain boundaries. Therefore, for each specimen, the three highest and lowest hardness values were considered as candidates for the soft (α) and hard (β) phase, which can be seen in table 2. Here, measurements identified as *As-Received*-3 and *Aged*-3 were rejected because they were too low compared to measurements 1 and 2 for their respective specimens. These values were then averaged to obtain a representative hardness for the α and β phases, which were 225.362 and 580.768 for the as-received specimen and 201.253 and 501.154 for the aged sample. The loading curves for each hardness measurement and residual indent impressions for the *Aged*-2 and *Aged*-5 data points are shown in figure 2(e).

Afterward, the ratio of Vickers hardness in the α and β phases ($HV^{\alpha/\beta}$) was calculated as:

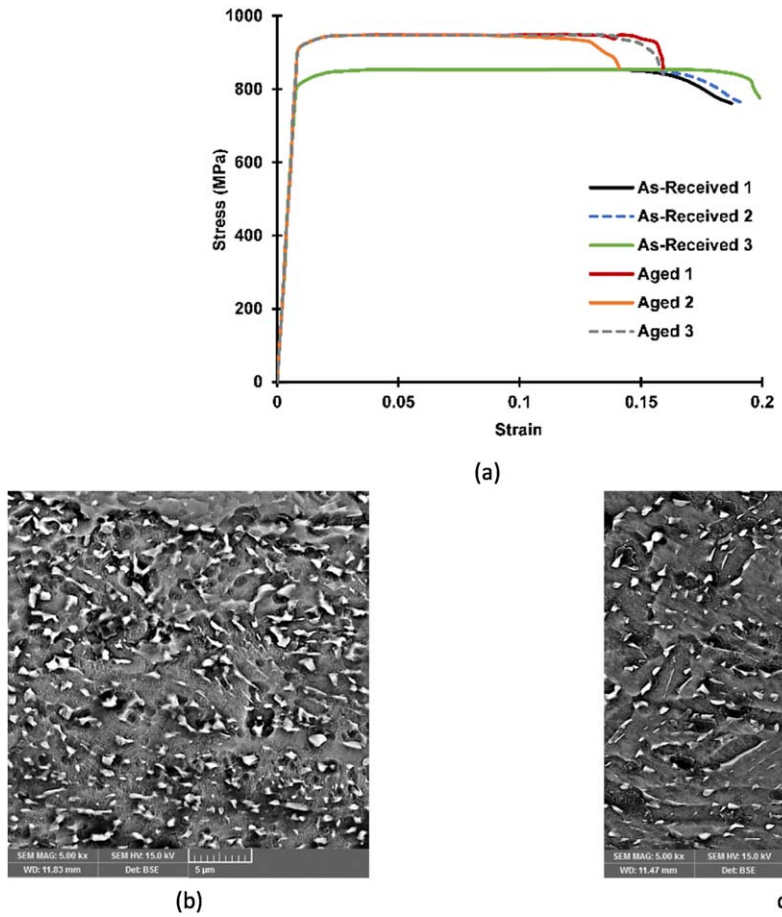

Figure 1. (a) Engineering stress-strain curves of as-received and aged Ti–6Al–4V alloy, (b) As-received BSE image with 5k magnitude, and (c) BSE Image of Aged Ti–6Al–4V alloy with 5k magnitude.

Table 2. Highest and lowest values of Vickers hardness obtained from micro-indentation tests on the as-received and aged specimens.

Identifier	Vickers Hardness	Remarks	Average Hardness
As-Received-1	587.961	Candidate for β.	580.768
As-Received-2	573.575	Candidate for β.	
As-Received-3	514.967	Rejected.	
As-Received-4	229.441	Candidate for α.	225.362
As-Received-5	225.077	Candidate for α.	
As-Received-6	221.568	Candidate for α.	
Aged-1	510.432	Candidate for β.	501.154
Aged-2	491.876	Candidate for β.	
Aged-3	445.333	Rejected.	
Aged-4	216.942	Candidate for α.	201.253
Aged-5	196.113	Candidate for α.	
Aged-6	190.705	Candidate for α.	

$$\text{As-Received: } \mathrm{HV}^{\alpha/\beta} = \frac{\mathrm{HV}^{\alpha}}{\mathrm{HV}^{\beta}} = \frac{225.362}{580.768} = 0.38$$
$$\text{Aged: } \mathrm{HV}^{\alpha/\beta} = \frac{\mathrm{HV}^{\alpha}}{\mathrm{HV}^{\beta}} = \frac{201}{501} = 0.40 \quad (1)$$

In section 2.3.2, this experimental finding is used for modeling the microstructure of dual-phase aged Ti–6Al–4V alloy.

2.3. Micromechanical modeling

2.3.1. Representative volume element

The SEM images of the microstructure of aged samples were processed using the image processing toolbox of Matlab software to produce a binary image with the same β phase fraction as obtained in the previous section (figure 3). The binary image, which is a 300*300 cropped picture out of the SEM image, marked as yellow in figure 3(a) was processed using an

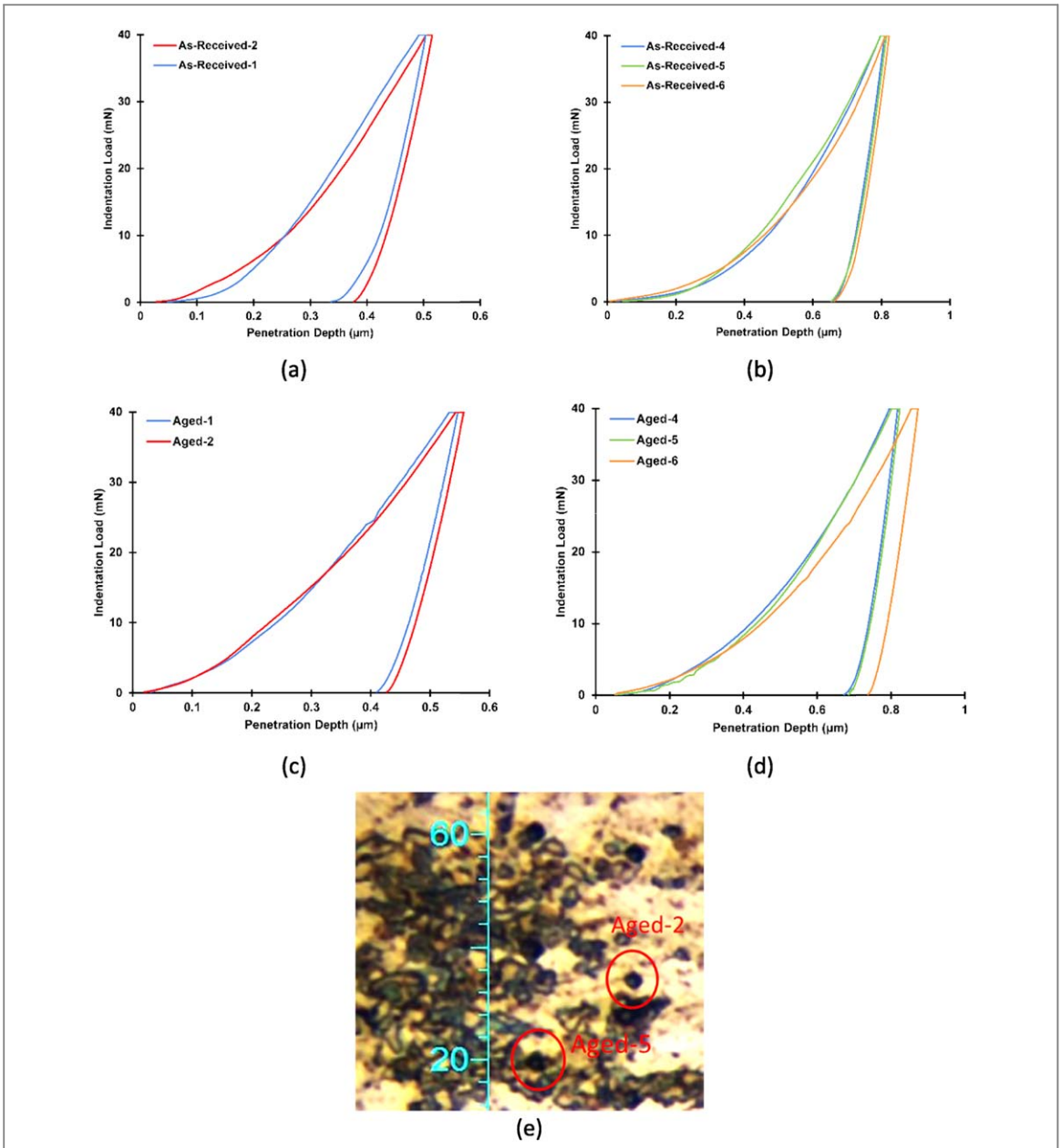

Figure 2. (a)–(d): The loading-unloading curves for the accepted Vickers hardness measurements in table 2, and (e) Residual indent impressions for the *Aged*-2 and *Aged*-5 data points (length units are in μm).

in-house Matlab code to create a two-dimensional (2D) finite element mesh for the Abaqus FE analysis software [40]. A total of 90 000 elements was used, which is well in the convergence region of the mesh study done in [41]. Based on [42], four-node 2D plane strain elements with reduced integration (CPE4R) were assigned to the FE mesh. The resulting RVE can be seen in figure 3(c), in which the green sections refer to the α phase, and the grey zones refer to the β phase.

2.3.2. Mechanical properties of the phases

The two phases in the microstructure were modeled as isotropic elastoplastic solids with similar elastic behavior. Their flow behavior was estimated using equation (2), which is based on the rule of mixtures (RoM), which was successfully employed in previous studies [20].

$$\begin{cases} \bar{\sigma}(\bar{\varepsilon}_p) = (1 - V_f^{\beta})\bar{\sigma}^{\alpha}(\bar{\varepsilon}_p) + V_f^{\beta}\bar{\sigma}^{\beta}(\bar{\varepsilon}_p) \\ \dfrac{\bar{\sigma}^{\alpha}(\bar{\varepsilon}_p)}{\bar{\sigma}^{\beta}(\bar{\varepsilon}_p)} = \dfrac{HV^{\alpha}}{HV^{\beta}} = HV^{\alpha/\beta} \end{cases} \quad (2)$$

In these equations, $\bar{\sigma}(\bar{\varepsilon}_p)$, $\bar{\sigma}^{\alpha}(\bar{\varepsilon}_p)$, and $\bar{\sigma}^{\beta}(\bar{\varepsilon}_p)$ refer to equivalent stresses as functions of equivalent plastic strain for the macroscopic specimen [43, 44], the α phase, and the β phase, respectively. HV^{α}, and HV^{β} are Vickers hardness values for the α and β phases and their ratio, $HV^{\alpha/\beta}$, in the aged samples was obtained experimentally in section 2.2 to be 0.4. Also, V_f^{β} is the volume fraction of the β phase and was obtained experimentally in section 2.1 to be averagely 15.2% in the aged samples of Ti–6Al–4V alloy.

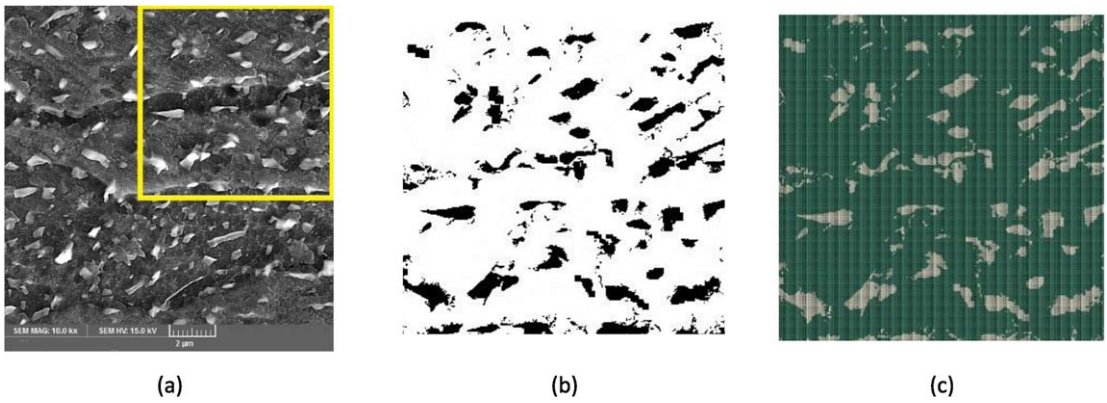

Figure 3. The procedure of the RVE creation from SEM images for simulation analysis. (a) SEM image of Aged Ti–6Al–4V alloy with 10k magnitude; (b) 300*300 binarized image of the microstructure created from the marked region of (a); (c) RVE model used in numerical simulation based on a 2D plane strain with 90,000 elements.

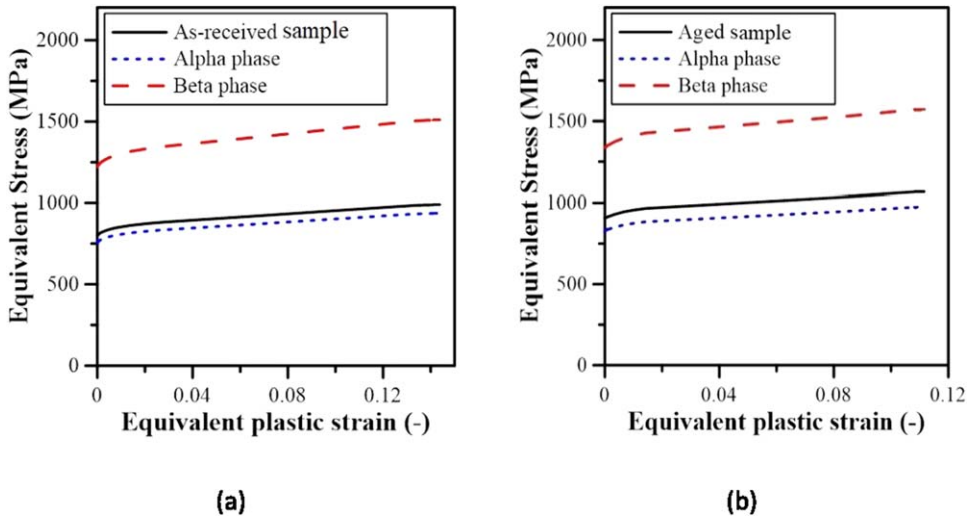

Figure 4. Flow curves of the macroscopic specimens and the α and β phases for (a) as-received and (b) aged Ti–6Al–4V alloy.

Experimental flow curve of as-received and heat-treated Ti–6Al–4V alloy along with their equivalent stress-strain curves of the matrix material of α and β phases, $\bar{\sigma}^{\alpha}(\bar{\varepsilon}_p)$, and $\bar{\sigma}^{\beta}(\bar{\varepsilon}_p)$, are plotted in figure 4 and were used as inputs for the FEA.

2.3.3. *The Gurson–Tvegaard–Needleman (GTN) damage model*

In Ti–6Al–4V alloys, the β phase is the hard phase and has the higher ultimate stress, for which elastoplastic modeling is sufficient. However, the α phase is soft and experiences ductile failure, which needs to be taken into consideration. A suitable damage model is the modified GTN model, formulated based on an isotropic material containing a single spherical void that contributes to the formulation of the yield equation [45]. In this model, the yield potential function describing the influence of void evolution on hardening is in the form of equation (3):

$$\phi = \left(\frac{\sigma_V}{\sigma_Y}\right)^2 + 2q_1 f^* \cosh\left(\frac{3}{2}\frac{q_2\sigma_H}{\sigma_Y}\right) - (1 + q_3 f^{*2}) = 0 \quad (3)$$

In this equation, σ_V, σ_H and σ_Y are the Von Mises equivalent stress, the hydrostatic stress, and the yield stress of the material and q_1, q_2, and q_3 are fitting parameters used to calibrate the model for experimental results. The function f^* accounts for the loss of load-bearing capacity based on the increase of void fraction (equation (4)).

$$f^*(f) = \begin{cases} f & \text{for } f \leqslant f_c \\ f_c + \dfrac{1/q_1 - f_c}{f_F - f_c}(f - f_c) & \text{for } f > f_c \end{cases} \quad (4)$$

Here, f is the void fraction, f_c and f_F are critical void volume fractions at the onset of coalescence and at the point of complete fracture [46]. Increase of void fraction proceeds by the growth of existing voids ($f_{\text{void growth}}$) and nucleation of new voids ($f_{\text{void nucleation}}$):

Table 3. GTN model parameters for Ti-6A-l4V.

Parameter	Meaning	Value(s)	Source
q_1	Determines the shape of the yield surface	1.5	[50]
q_2	Determines the shape of the yield surface	1	[50]
q_3	Determines the shape of the yield surface	2.25	[50]
f_0	Initial void fraction	1.0×10^{-6}	[27]
f_c	Critical void fraction	$(f_C, f_F) = \begin{cases} (0.04,\ 0.06) \\ (0.27,\ 0.32) \\ (0.50,\ 0.60) \end{cases}$	[27]
			[50]
f_F	Failure void fraction		[51]
f_N	Void nucleation rate	0.0007	[51]
		0.008	[50]
		0.06	[43]
ε_N	Void nucleation strain	0.2	[51]
		0.25	[50]
		0.3	[43]
S_N	Standard deviation on void nucleation strain	0.025	[50]
		0.1	[27]
		0.3	[43]

Table 4. DOE with four factors in three levels by the Taguchi method.

NO.	f_0	f_c	f_F	S_N	ε_N	f_N	Simulated Strain Values of Failure	Strain Differences
1	1×10^{-6}	0.04	0.06	0.025	0.25	0.0007	0.100 195	0.0525
2	1×10^{-6}	0.04	0.06	0.10	0.20	0.008	0.059 387	0.0933
3	1×10^{-6}	0.04	0.06	0.30	0.30	0.06	0.034 165	0.1185
4	1×10^{-6}	0.27	0.32	0.025	0.20	0.06	0.037 585	0.1148
5	1×10^{-6}	0.27	0.32	0.10	0.30	0.0007	0.144 872	0.0078
6	1×10^{-6}	0.27	0.32	0.30	0.25	0.008	0.088 017	0.0647
7	1×10^{-6}	0.50	0.6	0.025	0.30	0.008	0.084 459	0.0682
8	1×10^{-6}	0.50	0.6	0.10	0.25	0.06	0.039 089	0.1136
9	1×10^{-6}	0.50	0.6	0.30	0.20	0.0007	0.149 589	0.0028

$$\dot{f} = \dot{f}_{\text{void nucleation}} + \dot{f}_{\text{void growth}} = (1 - f).\ \dot{\varepsilon}_{kk} + \frac{f_N}{s_N\sqrt{2\pi}} \exp\left(-\frac{1}{2}\left(\frac{\bar{\varepsilon} - \varepsilon_N}{S_N}\right)^2\right)\dot{\bar{\varepsilon}} \quad (5)$$

where $\dot{\varepsilon}_{kk}$ is the volumetric plastic strain rate; f_N is the volume fraction of secondary voids; $\bar{\varepsilon}$ is the equivalent plastic strain; ε_N and S_N are mean value and standard deviation of the characteristic plastic strain distribution [47], respectively; and $\dot{\bar{\varepsilon}}$ is the equivalent plastic strain rate [48].

The GTN damage model relies on a large number of macroscopic and microscopic variables, which makes the calibration very difficult. In the GTN model outlined above, nine parameters have to be specified as properties of the material. These parameters and their respective values have been defined in table 3. Values for q_1, q_2, and q_3, which are the most important parameters [49], have been extracted from previous studies [49] and [50]. Guzman *et al* [27] reported very low (1.0×10^{-6}) values for f_0 which has also been used in this study. Different values for the critical void fraction (f_c) of Ti–6Al–4V alloy have been used in the literature. In this study, three values (0.04, 0.27, and 0.50) have been applied for the void fraction. Failure void fraction (f_F) can be determined based on f_c, so the values (0.06, 0.32, and 0.6, which are based on the previous studies as referred in the table below) have been used as well. The other three parameters which are f_N, ε_N and S_N have been optimized using the Taguchi method in section 2.3.4.

2.3.4. Design of experiment using the Taguchi method

The Taguchi DOE is one of the best methods for analyzing multiple variables. In this method, the most effective parameters are chosen as inputs. In the current study, failure void fraction (f_F), void nucleation rate (f_N), void nucleation strain (ε_N) and standard deviation of void nucleation strain (S_N) are the variables with values, as discussed in the previous section. Nine trials were determined using Matlab software based on 3-level 4-factor design and carried out using FEA. The details of these trials are reported in table 4.

In order to quantify the results of each trial and find the most optimal set of parameters, the root-mean-squared error (RMSE) between experimental and predicted stress values was calculated for each trial, according to equation (6).

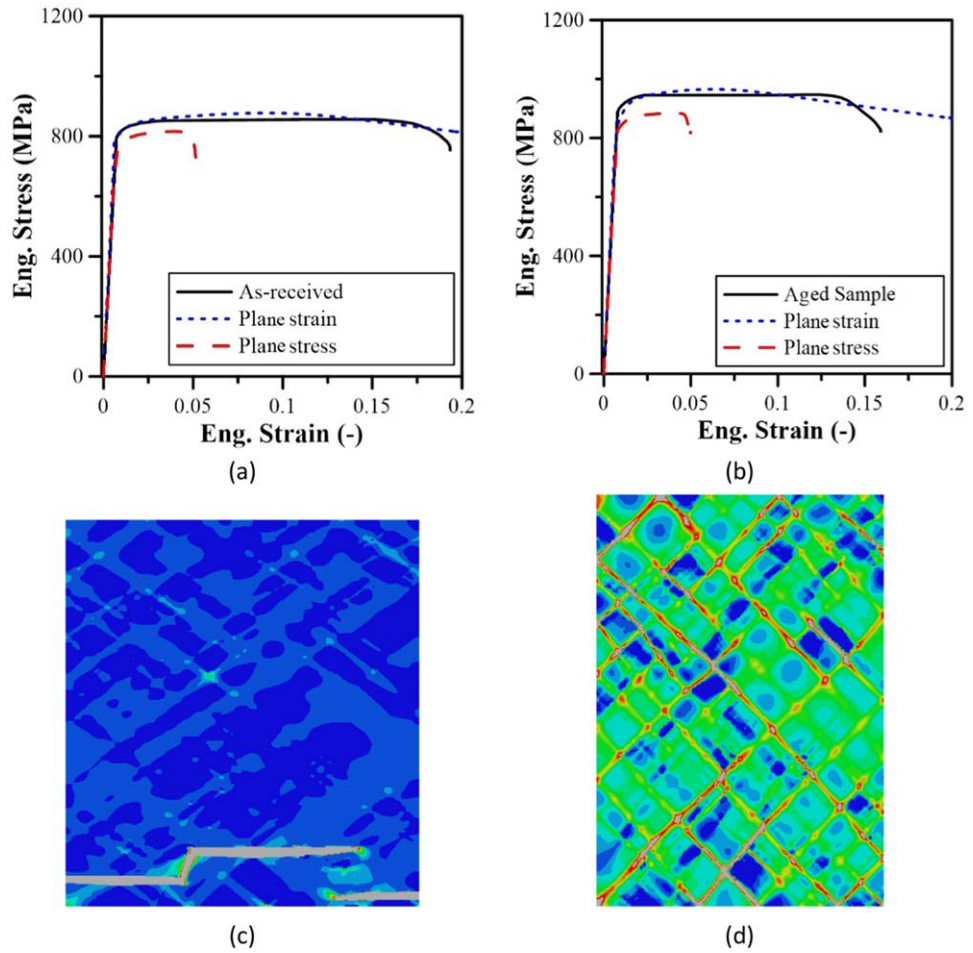

Figure 5. Effect of element type on simulation results; Plane-strain and plane-stress strain results for as-received (a) and aged (b) specimens; Contour plot of equivalent plastic strain for the as-received specimen under plane strain (c) and plane stress (d) conditions.

$$\mathrm{RMSE} = \sqrt{1/\mathrm{n}\sum_{\mathrm{j}=1}^{\mathrm{n}}(\mathrm{y_i} - \mathrm{y_j})^2} \qquad (6)$$

Where y_i is the stress value predicted using FEA and (y_j) is the experimentally observed value at that strain, and n is the number of strains in which this measurement was taken.

3. Results and discussion

3.1. Choice of element type

Figures 5(a) and (b) show the stress-strain response of plane stress and plane strain simulations for the as-received and aged specimens without considering the damage. In both cases, the plane stress model underestimates the yield stress and results in early failure. Evidently, the plane strain model predicts the experiment stress-strain results more accurately. However, as it is evident in figures 5(c) and (d), the plane strain condition fails to fully capture the effect of voids in the microstructure.

3.2. Calibration of damage parameters

Nine trials with various combinations of GTN damage model parameters were conducted as designed using the Taguchi method with the help of Matlab software. 'Failure strain values' were determined to be the response or the output of the trials. This set of parameters plays a very significant role in attaining the optimized variables, for a better damage model, and is obtained from the finite element simulations. Details of the trials and their results are listed in table 4.

The optimization procedure was done based on the failure strain. The trial with the minimum difference between the simulated failure strain and the experiment was selected as the optimal one. Figure 6 illustrates the stress-strain curves of the trials designed using the Taguchi method. Trial 9 with $f_F = 0.6$, $S_N = 0.3$, $\varepsilon_N = 0.2$ and $f_N = 0.0007$ has a minimum difference with the experiment ($\Delta\varepsilon = 0.0028$).

Figure 7 depicts the plot of main effects for means of the 4-factor-3-level Taguchi experimental design. This shows that each parameter has its consequence on the failure strain. According to the final results, f_N as representative of the void nucleation rate is the most influential parameter. The effects of f_F, S_N, and ε_N, on the other hand, are comparatively small.

At the level of inclusions, the f_N parameter embodies the void volume fraction nucleated in the material [24]. It can be assumed that not only adding

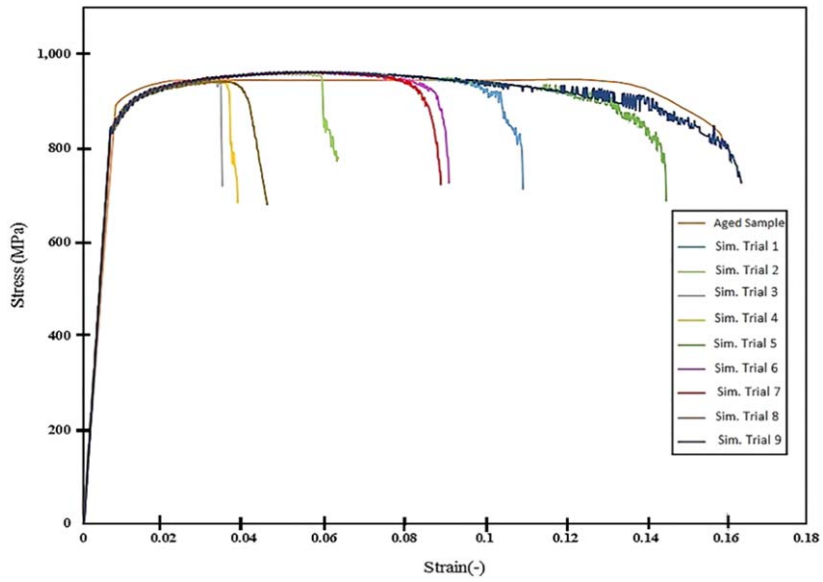

Figure 6. Stress-strain curves of selected trials by Taguchi method.

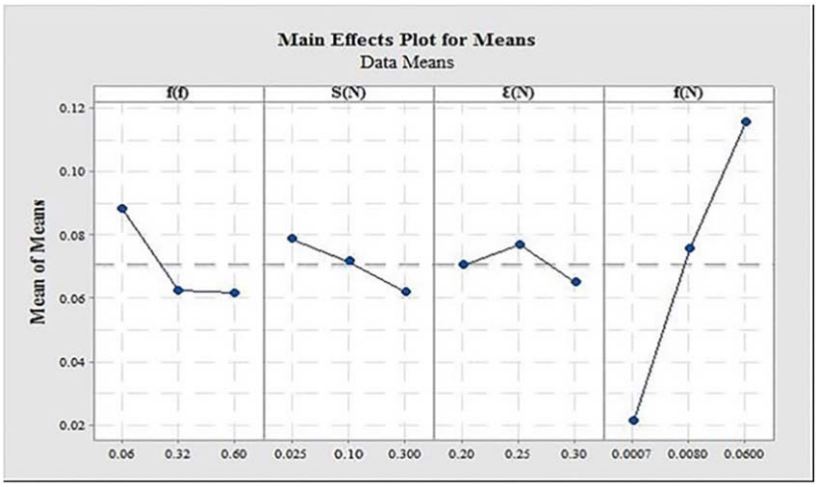

Figure 7. The plot of main effects for means of the 4-factor-3-level Taguchi experimental design in Matlab software.

Table 5. Optimal damage parameters for the aged specimen.

q_1	q_2	q_3	f_0	f_c	f_F	S_N	ε_N	f_N
1	1.5	2.25	1×10^{-6}	0.5	0.6	0.3	0.3	7×10^{-4}

up the values of f_N leads to the void initiation, but also could it increase the load reduction rate, specifically after necking [9]. The number of cavities in the matrix is also represented by this parameter. Hence, the higher the values of f_N can get, the earlier the failure of the specimen will occur. As reported in [24], by the increment of f_N, while the slope of all the stress-strain curves after fracture initiation has been considered constant, the mechanical properties are affected and weakened. For low loads, this leads to rapid degradation of the load and voids initiation [52].

Based on the results in figure 7 using the Taguchi Method, optimal damage parameters are suggested, which have been listed in table 5. It can be observed from figure 8 that this set of parameters can model the stress-strain response very well with an even fewer RMSE in comparison with the nine trials demonstrated in figure 6, with nearly a 3% error.

3.3. Damage initiation and progression

Figure 9 shows the evolution of damage in the modeled RVE at various values of equivalent plastic strain. It is

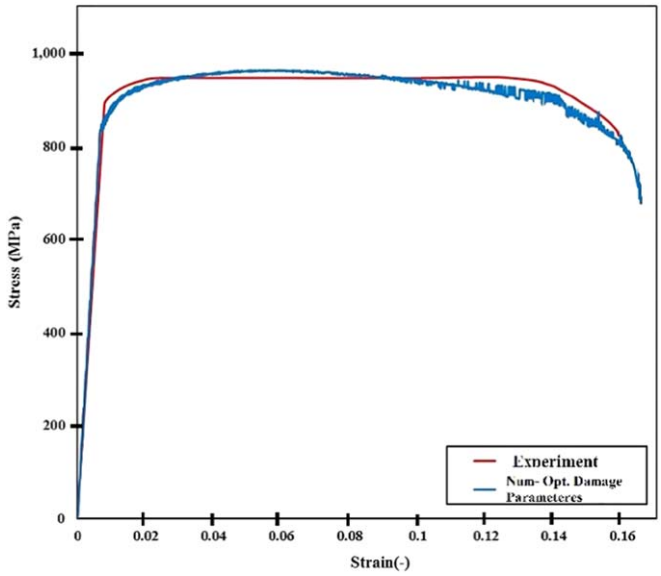

Figure 8. Stress-Strain response of micromechanical simulation with optimized damage parameters versus the experimental engineering stress-strain curve of the aged Ti–6Al–4V alloy sheet.

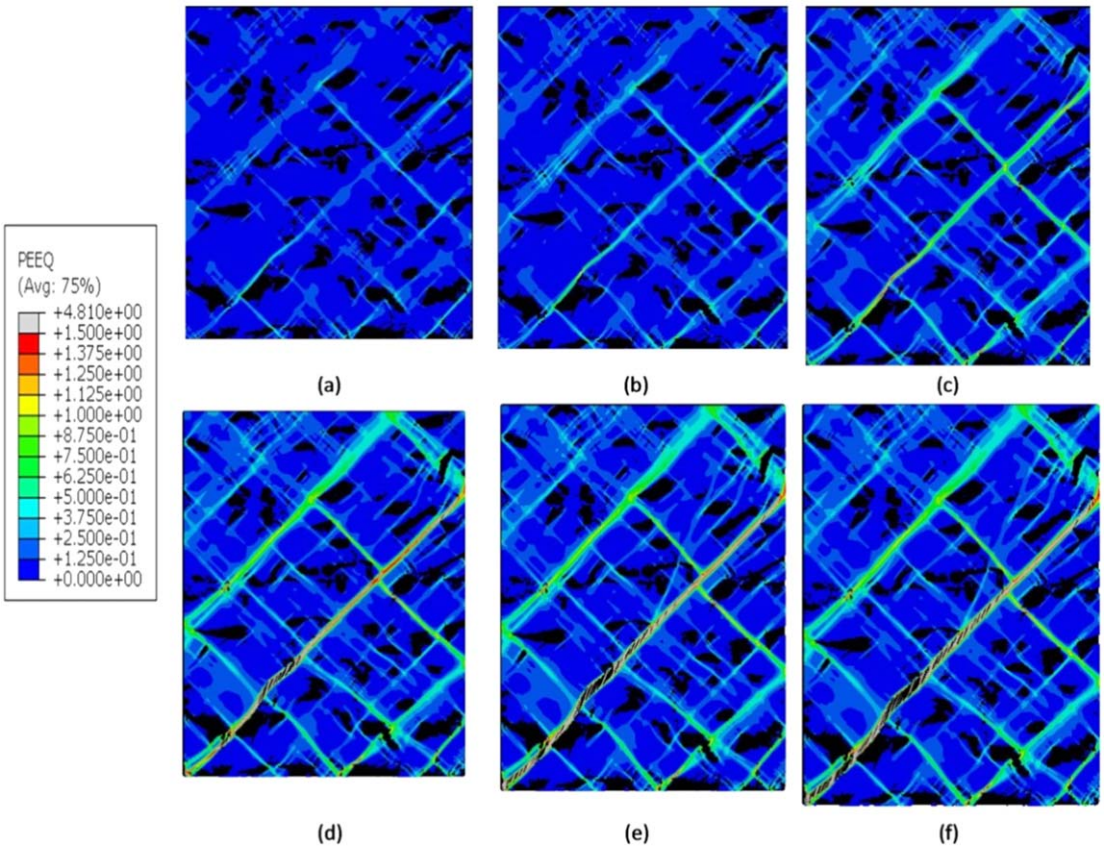

Figure 9. Damage initiation and evolution in the micromechanical model of aged Ti–6Al–4V alloy, via employing the optimized parameters of the GTN model, along with the distributions of plastic equivalent strain (PEEQ) with increasing the tensile strain values.

evident that the usual damage mechanism of initiation, propagation, and coalescence occurs.

The formation of shear bands is consistent with the ductile fracture. Stress inhomogeneity in the interface of hard and soft phases causes shear bands to originate in the interface [53], which then collides and grows in the softer phase (α), leading to coalescence and final failure. It can be observed that stress does not penetrate the β phase, validating the absence of damage and thus showing that modeling damage in

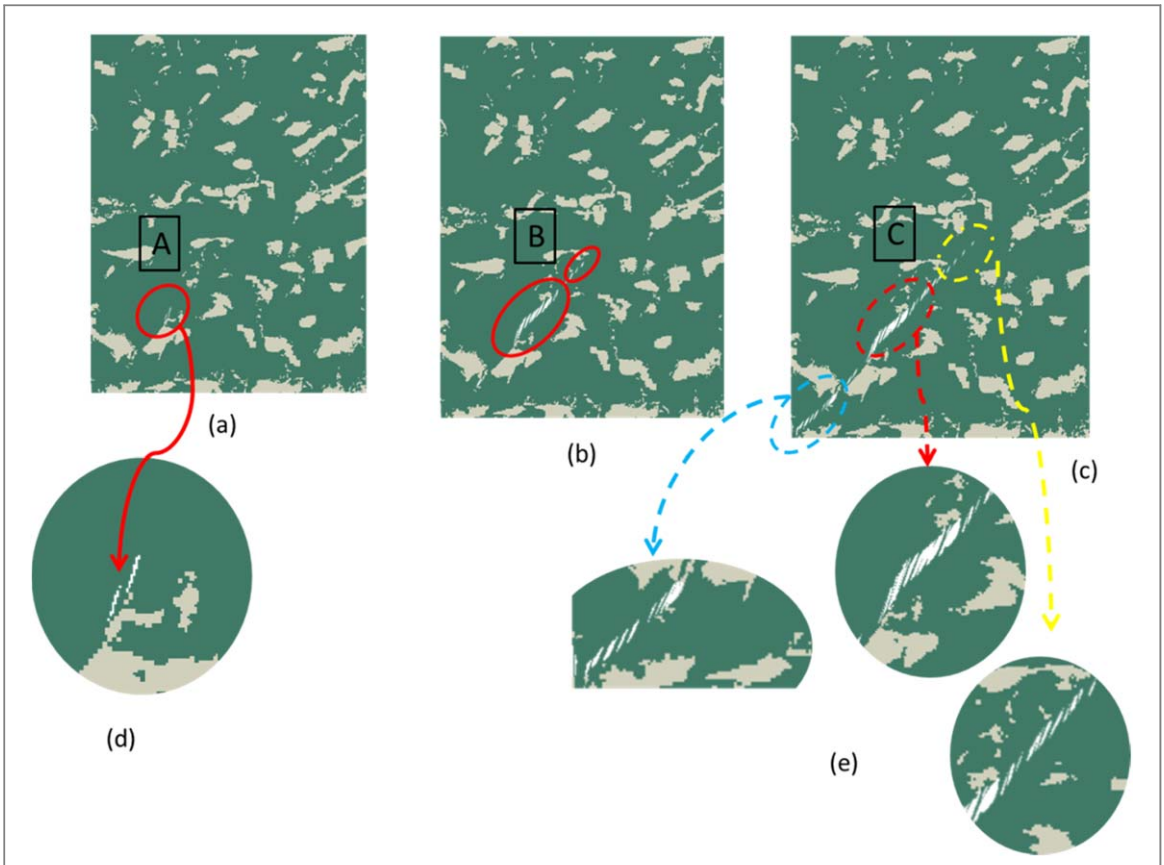

Figure 10. (a)–(e) Damage initiation and evolution in the micromechanical model of aged titanium grade 5 along with the plastic strain in the damaged model after the contour elimination. (f) Detailed view of the shear band presence in the fracture surface of the aged sample.

the α phase was a valid choice. Furthermore, according to figure 8(b), numerically predicted and experimental stress-strain curves coincide very well with a three percent error. This could indicate that the scalar damage variables of the GTN model can describe the deformation behavior adequately in the dual-phase titanium. The results show that the failure pattern is not severely deviating from classical ductile failure observations. However, it was detected that the relatively low deformation of β grains causes high deformation localization in the surrounding α matrix, which plays a vital role in the final failure of the material. Furthermore, it is expected that the specific crystallographic orientation of α grains nearby the β phase influences the possibility of damage initiation and propagation [54].

The evolution of damage is better visualized on the deformed geometry without contours (figures 10(a)–(e)). It is observed that damage initiates at region A in figure 10(a). While this continues to propagate in figure 10(b), other regions such as B start to initiate (the initiation area has been magnified in figure 10(e)). In figure 10(c), it is shown that damaged bands initiated in marked sites coalesce. Finally, in figure 10(d), they continue to grow and coalesce with the damage occurring at site C, which results in the final failure of the structure. The shear bands marked by the colored circles are magnified in figure 10(e). An SEM image (figure 10(f)) has been mentioned here as well, to verify the simulation results from the shear-band point of view, and the assumption that was discussed in section 3.1, that failure starts near the β phase with increasing the load [55].

3.4. Final failure mechanism

Figure 11 shows the strain distribution before the final failure. The results show similar damage mechanisms as reported in previous studies, focusing on the role of crack pattern in the mechanical failure of metals [56]. The stress field in the microstructure could lead to void growth in shear bands, which could cause final failure [57].

3.5. Analysis of fracture surfaces

Figure 12 shows the SEM images of fracture surfaces of as-received and aged specimens. In all SEM images representing the fracture morphologies, the cup-cone shapes are evident, which indicate the obvious necking [58]. It can be observed that the as-received sample contains a number of dimples [59]. The presence of a few voids, as marked in the magnified SEM image (figure 12(c)) [60] in the fracture surface of the aged sample, indicates that the primary failure mechanism in this specimen could be the void coalescence [61]. The dimples in the aged specimen are smaller than the dimples found in as-received samples, and more

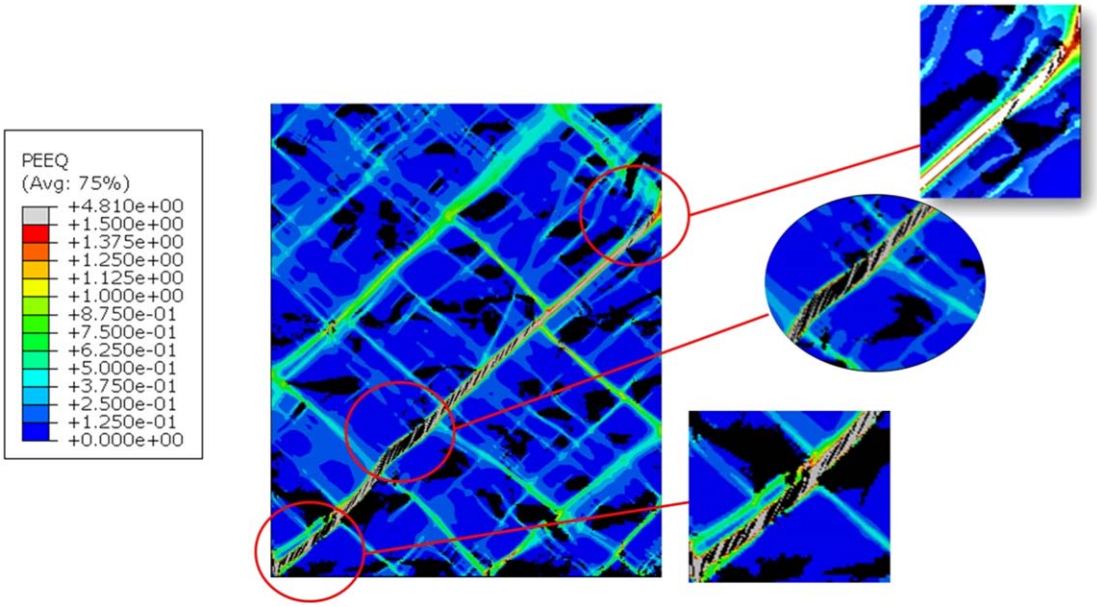

Figure 11. The equivalent plastic strain at failure.

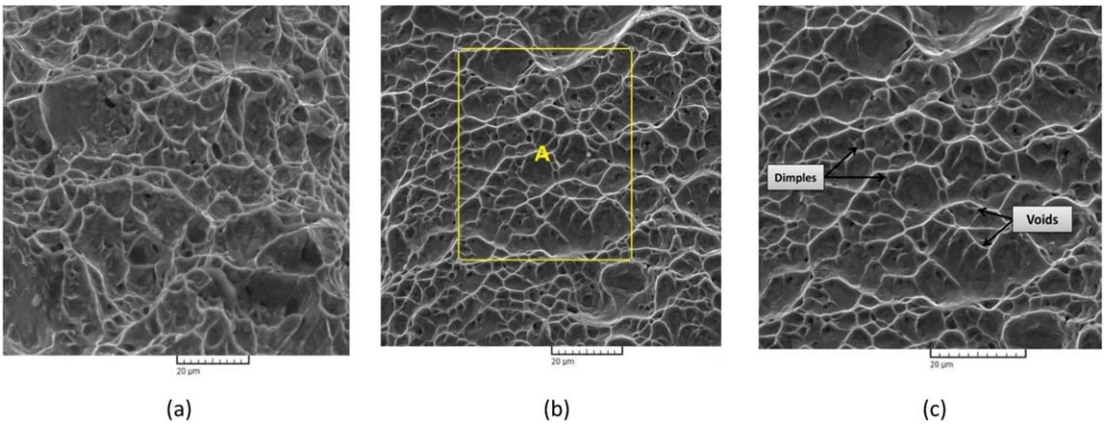

Figure 12. The fracture surface of (a) As-received with 2000× magnification, (b) Aged specimen under SEM with 1500× magnification, and (c) 2000× magnified image of the fracture surface of the aged sample (Marked as (A) in figure 12(b)).

homogenous dispersion of dimples from the size and shape point of view could be depicted. The homogeneity of shear bands is also evident in the heat-treated samples, as discussed in figure 10(a). These properties can account for the increase in strength seen in the stress-strain curve [62].

As was evident in figure 1 aged sample had lower ductility than the as-received specimens. This phenomenon can be explained using fractography images. This low ductility is aligned with an intergranular dimple rupture. Therefore, the formation of dimples due to the strain localization can explain this lower ductility [63].

4. Conclusion

In this paper, failure and damage mechanisms in as-received and aged Ti–6Al–4V bio-alloy under tensile loading were investigated using experiments and finite element analyses. The objective of this study was to obtain a set of parameters for successful micromechanical simulation of the tensile behavior of Ti–6Al–4V alloy using experimental and numerical methods. Tensile tests and micro-hardness measurements were utilized alongside the rule of mixtures (RoM) to obtain flow curves for the α and β phases. SEM imaging was used to determine phase fractions and to create RVEs. Furthermore, the GTN damage model was calibrated using the Taguchi DOE method in order to predict damage in the microstructure, and the results were correlated with fracture surfaces obtained using fractography to investigate the failure mechanism.

The main conclusions of this study are as follows:

1. The Taguchi DoE method was successfully used for calibration of the GTN damage model, and its

use significantly reduced the number of performed simulations. The final numerically predicted stress-strain curve predicted the experiment very well with an RMSE of 3%.

2. Based on the Taguchi method and in the investigated material, rate of void nucleation (f_N) was the most influential parameter in the GTN model. The effects of f_F, S_N, and ε_N were comparatively small.

3. The damage mechanism of initiation, propagation, and coalescence occurred in the specimens. Stress inhomogeneity in the interface of hard and soft phases caused shear bands to originate in phase boundaries and then grow in the softer phase, leading to coalescence and final failure. The formation of shear bands was consistent with the ductile fracture, and the absence of damage in the β phase supported the use of the GTN damage model.

4. Analyses of the fracture surface show few voids and equiaxed homogenous dimples in the aged sample, meaning that the primary failure mechanism in this specimen is void coalescence, which supports the occurrence of ductile fracture, predicted by the simulations.

ORCID iDs

Shima Rastgordani https://orcid.org/0000-0001-5104-4597
Ali Ch Darabi https://orcid.org/0000-0001-9460-7572
Javad Kadkhodapour https://orcid.org/0000-0002-5106-2098
Seyed Reza Hamzeloo https://orcid.org/0000-0002-5476-1863
Mohammadreza Khoshbin https://orcid.org/0000-0002-2239-1706
Siegfried Schmauder https://orcid.org/0000-0001-6022-3853
Javad Mola https://orcid.org/0000-0002-9057-3114

References

[1] Geetha M, Singh A K, Asokamani R and Gogia A K 2009 Ti based biomaterials, the ultimate choice for orthopaedic implants—a review *Prog. Mater Sci.* **54** 397–425
[2] Zhechao F and Hongwei F 2018 Study on selective laser melting and heat treatment of Ti-6Al-4V alloy *Results in Physics* **10** 660–4
[3] Maimaitiyili T, Woracek R, Neikter M, Boin M, Wimpory R C, Pederson R, Strobl M, Drakopoulos M, Schäfer N and Bjerkén C 2019 Residual lattice strain and phase distribution in Ti–6Al–4V produced by electron beam melting *Materials (Basel)* **12** 1–20
[4] Wang C, Zhang G, Li Z, Zeng X, Xu Y, Zhao S, Hu H, Zhang Y and Ren T 2019 Tribological behavior of Ti–6Al–4V against cortical bone in different biolubricants *J. Mech. Behav. Biomed. Mater.* **90** 460–71
[5] Cui C, Hu B, Zhao L and Liu S 2011 Titanium alloy production technology, market prospects and industry development *Mater. Des.* **32** 1684–91
[6] Barriobero-Vila P 2010 *Effect of Heat Treatments on the Microstructure of Deformed Ti–6Al–4V 69* Vienna University of Technology https://publik.tuwien.ac.at/files/PubDat_215998.pdf
[7] Lu Y, Aristizabal M, Wang X, Pang B, Chiu Y L, Kloenne Z T, Fraser H L and Loretto M H 2019 The influence of heat treatment on the microstructure and properties of HIPped Ti–6Al–4V *Acta Mater.* **165** 520–7
[8] Liang Z, Sun Z, Zhang W, Wu S and Chang H 2019 The effect of heat treatment on microstructure evolution and tensile properties of selective laser melted Ti6Al4V alloy *J. Alloys Compd.* **782** 1041–8
[9] Yan X *et al* 2018 Effect of heat treatment on the phase transformation and mechanical properties of Ti6Al4V fabricated by selective laser melting *J. Alloys Compd.* **764** 1056–71
[10] Fan Z and Feng H 2018 Study on selective laser melting and heat treatment of Ti–6Al–4V alloy *Results Phys.* **10** 660–4
[11] Hou Y, Cai S, Sapanathan T, Dumon A and Rachik M 2019 Micromechanical modeling of the effect of phase distribution topology on the plastic behavior of dual-phase steels *Comput. Mater. Sci.* **158** 243–54
[12] Basantia S, Singh V, Bhattacharya A, Khutia N and Das D 2018 Prediction of tensile behaviour of ferrite-martensite dual phase steel using real microstructure-based RVE simulations *Mater. Today Proc.* **5** 18275–80
[13] Barbosa G C, Moreira L P, da Silveira L B, da Silva F R F and Cardoso M C 2018 Micromechanical modeling of dual-phase DP600 steel sheet plastic behavior based on a representative volume element defined from the real microstructure *Mater. Sci. Forum* **930** 293–8
[14] Amirmaleki M, Samei J, Green D E, van Riemsdijk I and Stewart L 2016 3D micromechanical modeling of dual phase steels using the representative volume element method *Mech. Mater.* **101** 27–39
[15] Kolli R and Devaraj A 2018 A review of metastable beta titanium alloys *Metals (Basel)* **8** 506
[16] Cao Y, Xue Z, Chen X and Raabe D 2008 Correlation between the flow stress and the nominal indentation hardness of soft metals *Scr. Mater.* **59** 518–21
[17] Sundararajan G and Tirupataiah Y 1994 The hardness-flow stress correlation in metallic materials *Bull. Mater. Sci.* **17** 747–70
[18] Takakuwa O, Kawaragi Y and Soyama H 2013 Estimation of the yield stress of stainless steel from the Vickers hardness taking account of the residual stress *J. Surf. Eng. Mater. Adv. Technol.* **03** 262–8
[19] Nayebi A, El Abdi R, Bartier O and Mauvoisin G 2002 New procedure to determine steel mechanical parameters from the spherical indentation technique *Mech. Mater.* **34** 243–54
[20] Ohata M, Suzuki M, Ui A and Minami F 2010 3D-Simulation of ductile failure in two-phase structural steel with heterogeneous microstructure *Eng. Fract. Mech.* **77** 277–84
[21] Tvergaard V and Needleman A 1984 Analysis of the cup-cone fracture in a round tensile bar *Acta Metall.* **32** 157–69
[22] Xu F, Zhang H, Zhao S, Chen Ch, Cao M and Chen W 2018 Optimized Calibration Procedure of the Damage Parameters of 6082-T6 Sheets *Materials* **11** 248
[23] Impaction E, Feng F, Li J, Yuan P, Zhang Q, Huang P, Su H and Chen R 2018 Application of a GTN Damage Model Predicting the Fracture of 5052-O Aluminum Alloy High-Speed *Metals* **8** 761
[24] Slimane A, Bouchouicha B, Mohamed B and Slimane S 2015 Parametric study of the ductile damage by the Gurson–Tvergaard–Needleman model of structures in carbon steel A48-AP *Journal of Materials Research and Technology* **4** 217–23
[25] Cha W G and Kim N 2014 Quantification of micro-cracks on the bending surface of roll formed products using the GTN model *Met. Mater. Int.* **20** 841–50
[26] Allahverdizadeh N, Gilioli A, Manes A and Giglio M 2015 International journal of mechanical sciences an experimental

and numerical study for the damage characterization of a Ti–6AL–4V titanium alloy *Int. J. Mech. Sci.* **93** 32–47
[27] Guzmán C F, Tuninetti V, Gilles G and Habraken A M 2015 Assessment of Damage and Anisotropic Plasticity Models to Predict Ti–6Al–4V Behavior *Key Engineering Materials* **651-653** 575–80
[28] Huez J, Feaugas X, Helbert A L, Guillot I and Clavel M 1998 Damage Process in Commercially Pure α-Titanium Alloy without (Ti40) and with (Ti40-H) Hydrides *Metallurgical and Materials Transactions A* **29** 1615–28
[29] Cao X, Wei X, Li G, Hu C, Dai K, Guo J, Zheng G, Liu C, Shen C and Guo Z 2017 Strain sensing behaviors of epoxy nanocomposites with carbon nanotubes under cyclic deformation *Polym. (United Kingdom)* **112** 1–9
[30] Hößler D and Ernst M 2019 Optimization of a $TiSi_2$ formation based on PECVD Ti using DoE methodology *Solid. State. Electron.* **158** 51–8
[31] Hakimian E and Sulong A B 2012 Analysis of warpage and shrinkage properties of injection-molded micro gears polymer composites using numerical simulations assisted by the Taguchi method *Mater. Des.* **42** 62–71
[32] Sun Q, Chen J, Li X and Pan H 2014 Parametric study of edge crack of silicon steel strip in cold rolling based on a shear modified GTN damage model *Procedia Maerials Sci.* **3** 1632–7
[33] Kumar S, Prasad L, Kumar S and Kumar V 2019 Physico-mechanical and Taguchi-designed sliding wear properties of Himalayan agave fiber reinforced polyester composite *Journal of Materials Research and Technology* **8** 3662–71
[34] Obiko J O, Mwema F M and Shangwira H 2020 Forging optimisation process using numerical simulation and Taguchi method SN *SN Applied Sciences* **2** 713
[35] Mosleh A O, Mestre-Rinn P, Khalil A M, Kotov A D and Mikhaylovskaya A V 2020 Modelling approach for predicting the superplastic deformation behaviour of titanium alloys with strain hardening/softening characterizations *Mater. Res. Express* **7** 1591
[36] Li C, Chen J, Li W, Ren Y J, He J J and Song Z X 2016 Effect of heat treatment variations on the microstructure evolution and mechanical properties in a β metastable Ti alloy *J. Alloys Compd.* **684** 466–73
[37] Balasundar I, Raghu T and Kashyap B P 2019 Correlation between microstructural features and tensile properties in near-α titanium alloy IMI 834 processed in the $\alpha + \beta$ regime *Mater. Perform. Charact.* **8** 932–45
[38] Lin Y C, Tang Y, Zhang X Y, Chen C, Yang H and Zhou K C 2019 Effects of solution temperature and cooling rate on microstructure and micro-hardness of a hot compressed Ti–6Al–4V alloy *Vacuum* **159** 191–9
[39] Kadkhodapour J, Schmauder S, Raabe D, Ziaei-Rad S, Weber U and Calcagnotto M 2011 Experimental and numerical study on geometrically necessary dislocations and non-homogeneous mechanical properties of the ferrite phase in dual phase steels *Acta Mater.* **59** 4387–94
[40] Zhang X, Zhong F, Shao J, Zhang C and Hou N 2016 Materials science & engineering a failure mechanism and mode of Ti–6Al–4V alloy under uniaxial tensile loading : experiments and micromechanical modeling *Mater. Sci. Eng. A* **676** 536–45
[41] Darabi A C, Chamani H R, Kadkhodapour J, Anaraki A P, Alaie A and Ayatollahi M R 2017 Micromechanical analysis of two heat-treated dual phase steels : DP800 and DP980 *Mech. Mater.* **110** 68-83
[42] Ramazani A, Mukherjee K, Quade H, Prahl U and Bleck W 2013 Materials science & engineering a correlation between 2D and 3D flow curve modelling of DP steels using a microstructure-based RVE approach *Mater. Sci. Eng. A* **560** 129–39
[43] Katani S, Madadi F, Atapour M and Rad S Z 2013 Materia ls and Design Micromechanical Modelling of Damage Behaviour of Ti—6Al—4V *Materials & Design* **49** 1016–21
[44] Ohata M, Suzuki M, Ui A and Minami F 2010 3D-Simulation of Ductile Failure in Two-Phase Structural Steel with Heterogeneous Microstructure *Engineering Fracture Mechanics* **77** 277–84
[45] Steglich D 1998 Micromechanical modelling of damage and fracture of ductile materials *Fatigue Fract. Eng. Mater. Struct.* **21** 1175–88
[46] Zhai J, Luo T, Gao X, Graham S M, Baral M, Korkolis Y P and Knudsen E 2016 Modeling the ductile damage process in commercially pure titanium *Int. J. Solids Struct.* **91** 26–45
[47] Farahani B V, Amaral R, Belinha J, Tavares P J, Moreira P and Frias R 2017 Sciencedirect sciencedirect sciencedirect a GTN failure analysis of an AA6061-T6 Bi-failure specimen a Portuguese GTN failure analysis of an AA6061-T6 thermo-mechanical modeling a high pressure blade airplane gas turbine engine *Procedia Struct. Integr.* **5** 981–8
[48] Li H, Fu M W, Lu J and Yang H 2011 Ductile fracture: experiments and computations *Int. J. Plast.* (https://doi.org/10.1016/j.ijplas.2010.04.001)
[49] Uthaisangsuk V, Prahl U and Bleck W 2008 Micromechanical Modelling of Damage Behaviour of Multiphase Steels *Computational Materials Science* **43** 27–35
[50] Verleysen P and Peirs J 2017 Quasi-static and high strain rate fracture behaviour of Ti6Al4V *Int. J. Impact Eng.* **108** 370–88
[51] Li H, Li J, Tang B, Fan J and Yuan H 2017 Simulation of intergranular ductile cracking in β titanium alloys based on a micro-mechanical damage model *Materials (Basel)* **10** 1–18
[52] Kossakowski P G 2010 An analysis of the load-carrying capacity of elements subjected to complex stress states with a focus on the microstructural failure *Arch. Civ. Mech. Eng.* **10** 15–39
[53] Yang D and Yang H 2018 Nanograin Formation within Shear Bands in Cold-Rolled Titanium *Nanocrystals and Nanostructures* ed C M Simonescu (Romania: Polytechnic University of Bucharest) 978-1-83881-511-0 (https://doi.org/10.5772/intechopen.76969)
[54] Mezzetta J, Choi J, Milligan J, Danovitch J, Chekir N, Bois-Brochu A, Zhao Y F and Brochu M 2018 Process-Property Relationships of Ti6Al4V Fabricated through Selective Laser Melting Department of Mining and Materials Engineering *International Journal of Precision Engineering and Manufacturing-Green Technology* **5** 605–12
[55] Lin Y C, Wu Q, Pang G D, Jiang X Y and He D G 2020 Hot tensile deformation mechanism and dynamic softening behavior of Ti–6Al–4V alloy with thick lamellar microstructures *Adv. Eng. Mater.* **22** 1–11
[56] Cheloee Darabi A, Guski V, Butz A, Kadkhodapour J and Schmauder S 2020 A comparative study on mechanical behavior and damage scenario of DP600 and DP980 steels *Mech. Mater.* **143** 103339
[57] Ayatollahi M R, Darabi A C, Chamani H R and Kadkhodapour J 2016 3D micromechanical modeling of failure and damage evolution in dual phase steel based on a real 2D microstructure *Acta Mech. Solida Sin.* **29** 95–110
[58] Lin Y C, Jiang X Y, Shuai C J, Zhao C Y, He D G, Chen M S and Chen C 2018 Effects of initial microstructures on hot tensile deformation behaviors and fracture characteristics of Ti–6Al–4V alloy *Mater. Sci. Eng. A* **711** 293–302
[59] Jiang Y Q, Lin Y C, Jiang X Y, He D G, Zhang X Y and Kotkunde N 2020 Hot tensile properties, microstructure evolution and fracture mechanisms of Ti–6Al–4V alloy with initial coarse equiaxed phases *Mater. Charact.* **163** 110272
[60] Wahed M A, Gupta A K, Sharma V, Mahesh K, Singh S K and Kotkunde N 2019 Material characterization, constitutive modelling, and processing map for superplastic deformation region in Ti–6Al–4V alloy *Int. J. Adv. Manuf. Technol.* **104** 3419–38
[61] Gasson P C 2006 *Light Alloys: From Traditional Alloys to Nanocrystals* 4th edn (Linacre House, Jordan Hill, Oxford, OX2 8DP, UK: I. Polmear Elsevier Butterworth-Heinemann) p 421 Illustrated. £49.99
Gasson P C 2006 *Aeronaut. J.* **110** 394–425
[62] Pardoen T and Hutchinson J W 2004 An Extended Model for Void Growth and Coalescence *Journal of the Mechanics and Physics of Solids* **48**
[63] International A 1987 *ASM Handbook Volume 12: Fractography* (United States: American Society for Metals) 978-0-87170-018-6